# MEASURED RCS POLAR CONTOUR MAPS FOR CODE VALIDATION

C.L. Larose
S.R. Mishra
David Florida Laboratory
Canadian Space Agency
Ottawa, Canada

C.W. Trueman
EMC Laboratory
Concordia University
Montreal, Canada

*ABSTRACT. Measured radar cross-section(RCS) data as a function of the angle of incidence and of the frequency over a wide range provide an excellent basis for code validation. This paper examines the RCS of six targets measured as a function of the angle of incidence of the plane wave, and of the frequency, through and beyond the resonance range of target size. The RCS is presented as a function of frequency and incidence angle using a color contour map in a polar format, with the radius proportional to the frequency. Such polar contour maps exhibit striking patterns. This paper relates such patterns to the underlying scattering mechanisms and target geometry. The RCS as a function of incidence angle and frequency is available from the authors for an extensive collection of targets.*

## 1. INTRODUCTION

Developers of new computer codes in computational electromagnetics carry out "code validation", in which computations are compared with reference data, both to demonstrate how accurately the code can solve a given problem, and to identify requirements of the code, such as the minimum number of elements per wavelength distance. In the literature, scattering codes are often validated by comparing monostatic or bistatic scatter patterns with measurements at a single frequency. A thorough evaluation of a computer code includes comparisons over a wide frequency range, to try to establish the limits of the validity of the code[1].

The open literature makes available the RCS as a function of frequency for only a few targets, such as a square plate from $0.25\lambda$ to $1.1\lambda$ in size[2], a metallic strip $0.53\lambda$ tall and from $0.5\lambda$ to $1.3\lambda$ in length[3], a metallic cube from $0.1\lambda$ to $3.7\lambda$ in size[4], each for only one angle of incidence. Our initial RCS measurements extended this set of "canonical" targets to include metallic strips and rods, over a 9 to 1 frequency range, for one or two individual angles of incidence such as broadside or end-on[5], for the validation of computations by wire-grid modeling and by the finite-difference time-domain method[6]. We then undertook to build a data base of measured radar cross-sections for over a hundred shapes, including discs, right-circular cones, cone-spheres, ellipsoids, pyramids, and simplified aircraft and ships[7]. For each target the RCS has been measured over a 9 to 1 frequency range, at one degree angle steps over 360 degrees when there is no axis of symmetry, or 180 degrees when there is one symmetry axis, and so forth. The measured RCS as a function of both frequency and incidence angle permits both the comparison of the measured RCS with the computed RCS as a function of frequency at a given incidence angle, and the traditional comparison as a function of incidence angle at a given frequency, and so provides a comprehensive set of reference data for code validation for that target for plane wave incidence in one plane.

This paper presents the RCS of six of the targets in our data base. By graphing the RCS vs. frequency and angle as a color contour map in a polar format[8], intriguing patterns of maxima and minima are seen. This paper lends insight into these patterns by relating them to the scattering mechanisms of the target. Our measured RCS data may present a challenge to others to demonstrate that their computer codes can accurately predict the scattering mechanisms suggested by our simple analysis.

### 1.1 Measured RCS

The scattered field is measured at the David Florida Laboratory in a 6 by 6 by 6 m anechoic chamber, using the setup shown in Fig. 1. The target is mounted on a styrofoam column on a rotator which can turn the target for $0 \le \theta \le 360$ degrees. The target is illuminated by a transmit horn and the scattered field measured by a receive horn. Hence the bistatic scattered field at a fixed range distance is measured. This section defines the bistatic, finite-range "radar cross-section" as graphed in this paper, and discusses its relationship to the true, monostatic RCS.

The transmit horn in Fig. 1 illuminates the target with a spherical wave of amplitude $E_i$ evaluated at the centre of

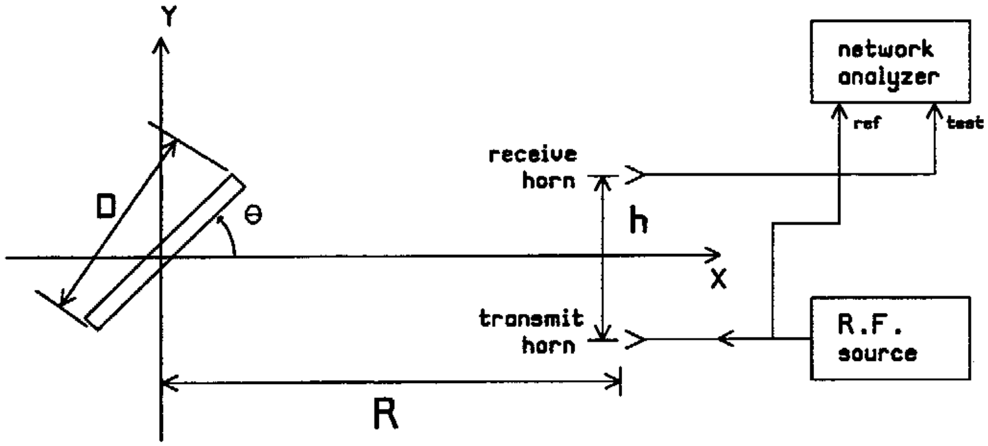

Fig. 1 The geometry of the measurement setup.

rotation. The target scatters field back to the receive horn, which measures field strength $E_t$, where the "t" subscript stands for or "target". The bistatic, finite range RCS, which we will also call the "measured RCS", is defined by

$$RCS(R,h,\theta,f) = 10\log\left(\frac{4\pi R^2 |E_t^2|}{|E_i^2|}\right) \qquad ...(1)$$

in dB, and depends on the horn separation $h$, the measurement range $R$, the angle of incidence, and the frequency. The calibration procedure for the measurement setup extracts $E_t$ from three voltages measured by the network analyzer: $V_1$ with the target on the support column; $V_2$ with a reference sphere on the support column, namely an 50.8 mm, highly-polished steel ball-bearing; and $V_3$ with nothing on the support column, representing the scattered field of the support column plus the residual scattered field of the anechoic chamber. Assuming that the target does not interact with the support column, the column-plus-room contribution can simply be subtracted. The "target response" is the difference at each frequency between the response with the target on the column, and that with nothing on the column, $V_t = V_1 - V_3$. Similarly, the "sphere response" is the difference between the response with the sphere on the column, and that with nothing on the column, $V_s = V_2 - V_3$. The scattered field at the location of the receive horn is proportional to the received voltage, hence for the target, $E_t = CV_t$, and for the sphere, $E_s = CV_s$, where $C$ is a complex-valued, frequency-dependent constant accounting for the gains of the horns, the losses and phase shifts in the cables, and so forth. To find the value of $C$ we evaluate the scattered field of the sphere $E_s = E_{Mie}$ using the Mie[9] series for plane wave scattering from a perfectly-conducting sphere, with the appropriate bistatic angle. Then $C = E_{Mie}/V_s$ and the scattered field of the target is

$$E_t = \left(\frac{E_{Mie}}{V_s}\right)V_t \qquad ...(2)$$

In using the Mie series for plane wave scattering from a sphere we are assuming that the measurement setup satisfies "far field" conditions, and we may be introducing a systematic error. Also we assume that the sphere is perfectly-conducting, which may not be appropriate for a steel sphere. Equations (1) and (2) define the "measured RCS" as graphed in this paper.

## 1.2 Geometric Error

The relationship between the "measured RCS" of Eqn. (1), based on the bistatic scattered field at finite range, and the true monostatic RCS is a complex one. Part of the difference between our measured RCS and the monostatic RCS is due to the bistatic, finite-range geometry, and we will call this the "geometric error", and part due to other sources of error[10]. True RCS measurement requires an incident plane wave, for which the field amplitude does not change with distance traveled, and for which the phase is constant in planes perpendicular to the direction of travel. In the measurement setup, the incident wave is spherical and so the illuminating field strength varies as inverse distance. Hence the part of the target nearest the horns is more strongly illuminated than that farthest from the horns. Also, the phase of the illuminating field is not uniform in planes perpendicular to the direction of propagation. And, the distances from various parts of the target to the receive horn differ from those associated with backscattered field, which alters the phase relationship of the scattered fields at

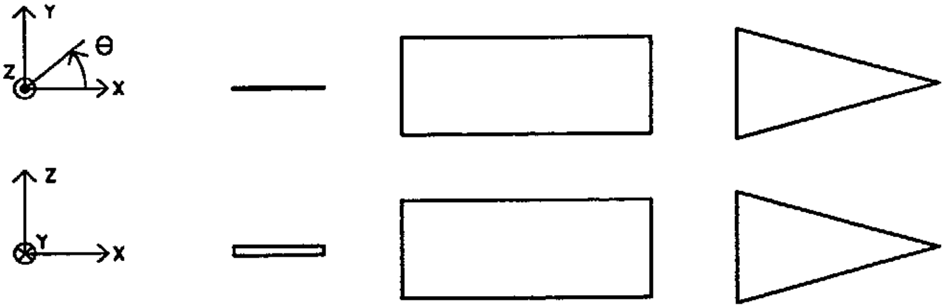

(a) thin strip (b) large rod (c) large cone

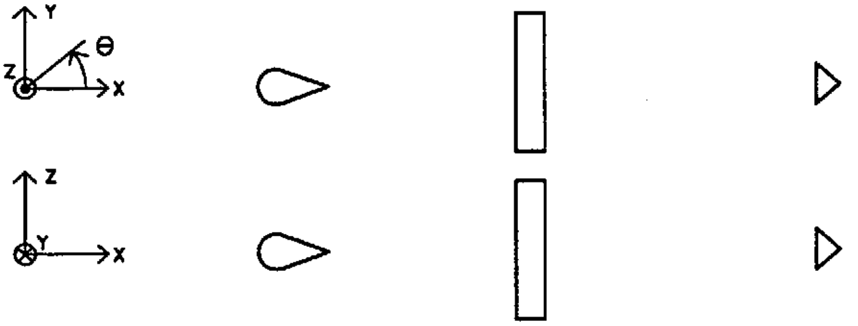

(d) cone–sphere (e) thick disk (f) small cone

Fig. 2 The relative sizes of the six targets, and their orientations in the coordinate system.

**Table 1**
The dimensions of each target, and the range distance and bistatic angle of the measurement.

| Target | Dimensions mm | Polarization | Bistatic angle degrees | Range m | D mm | $f_{max}$ GHz |
|---|---|---|---|---|---|---|
| thin strip | 63.6x6.36x0.32 | vertical | 8.3 | 1.2 | 63.9 | 44.1 |
| large rod | 177.8x71.1x71.1 | horizontal | 3.0 | 3.35 | 204.3 | 12.0 |
| large cone | 80.5 mm base diameter<br>147.6 mm length | horizontal | 7.7 | 1.295 | 153.0 | 8.3 |
| cone-sphere | 25.3 mm sphere diameter<br>50.1 mm overall length | horizontal | 8.2 | 1.217 | 50.1 | 72.7 |
| thick disk | 100.9 mm diameter<br>20.4 mm thickness | horizontal and vertical | 7.7 | 1.295 | 102.9 | 18.3 |
| small cone | 29.8 mm base diameter<br>17.85 mm length | vertical | 8.3 | 1.2 | 23.3 | 202.7 |

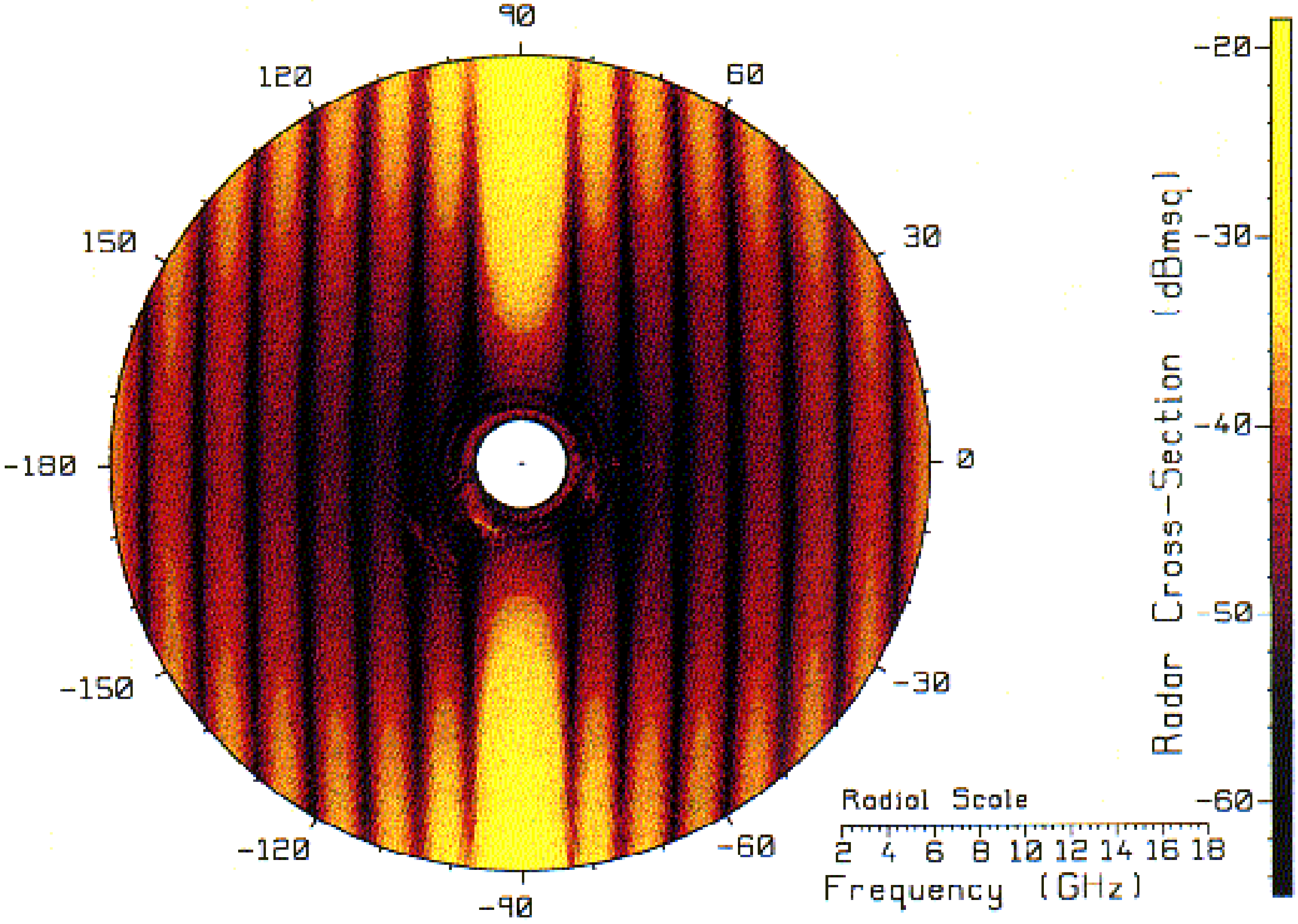

Fig. 3 The RCS of the thin strip of Fig. 2(a) for vertical polarization, with the incident electric field vector parallel to the $z$ axis. The RCS is shown with color contours as a function of the angle of incidence $\theta$ in the $xy$ plane, and of the frequency, with the radial axis proportional to the frequency, from 2 GHz at the inner circle to 18 GHz at the outer circle.

the location of the receiver. All these differences contribute to the geometric error.

If $D$ is the maximum diagonal dimension of the target, then if $R>>D$ and $R>>h$, the measurement setup approaches the conditions for monostatic RCS measurement, and we expect that the geometric error will be "small". The commonly-accepted "rule-of-thumb" for choosing a sufficiently large range $R$ to control the geometric error is[10]

$$R_{\min} = \frac{2D^2}{\lambda} \qquad \ldots(3)$$

where $\lambda$ is the wavelength. More elaborate minimum-range conditions are reviewed in [11]. Hence for a given target size $D$ and range $R$, the maximum frequency at which the rule-of-thumb is satisfied is

$$f_{\max} = \frac{Rc}{2D^2} \qquad \ldots(4)$$

where $c$ is the free-space speed of light. But the rule-of-thumb of Eqn. (3) does not provide an estimate of the geometric error in the RCS at that range.

Ref. [12] discusses the geometric error as follows. At a frequency and angle of incidence where the RCS has a maximum, small differences in the strength of the illumination and in the phase of the illumination of various scattering centers on the target, and small path differences back from the scattering centers to the receive horn, can be

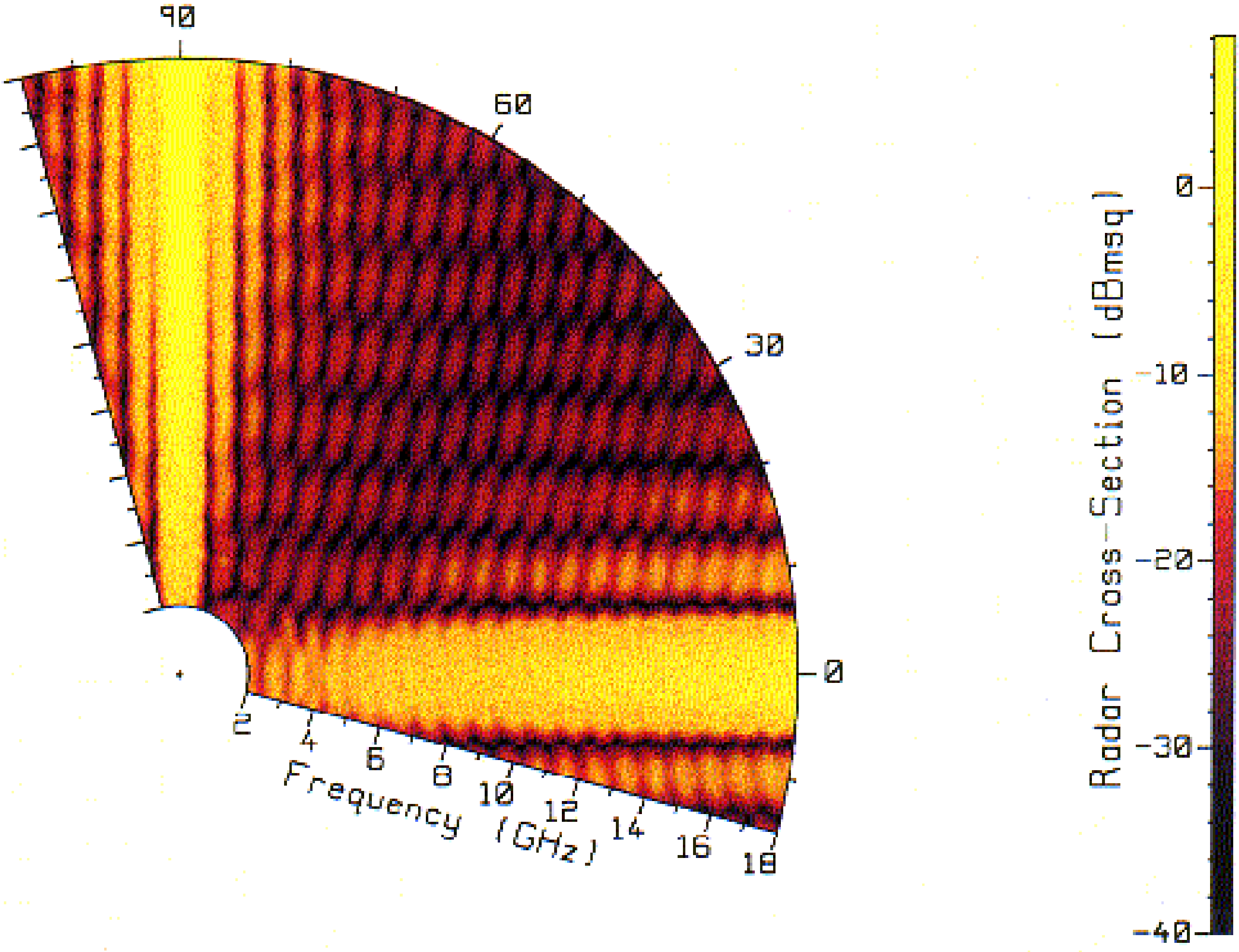

Fig. 4 The RCS of the large rod of Fig. 2(b) over one quadrant of the *xy* plane, for horizontal polarization, with the electric field vector parallel to the *xy* plane.

unimportant, and the error in the measured RCS compared to the monostatic RCS can be small. However minima in the RCS arise due to cancellation of the scattered field from various parts of the target, and then small differences in the strength and phase of the illumination, and in the path lengths back to the receive horn, can lead to very large errors in the RCS. Hence the geometric error in the RCS maxima can be small but that in the RCS minima large. Ref. [12] provides a tool for choosing the measurement range *R* and horn separation *h* to limit the geometric error to a preset maximum over a chosen range of RCS values below the maximum RCS.

The measured RCS contains other errors as well, associated with the signal-to-noise ratio, with the time-gating measurement method[10], with target alignment, and so forth[10,12]. We do not have a quantitative estimate of these errors in our measurements at this time. Dybdal[10] estimates the maximum achievable absolute accuracy in RCS measurement under carefully-controlled conditions as 0.5 dB.

For code validation purposes, comparisons of computations of the monostatic RCS against our measured RCS are approximate. Such comparisons will lead to good agreement in the RCS maxima, and differences in the minima. This is illustrated in Ref. [5], which compares the measured RCS of Eqn. (3) for the strip target of Fig. 2(a) with the computed monostatic RCS, from 2 to 18 GHz. The range and angle are given for the strip in Table 1. Excellent agreement is seen in Ref. [5] in the RCS maxima. However, the sharp, deep minima differ between the measurement and computation.

To make the best use of our measured bistatic, finite-range RCS data for code validation, the measurement setup of Fig. 1 should be simulated in the computation. This is easily done by locating a point source at the position of the feed horn, and computing the scattered field at the location of the receive horn. Then the measured and computed scattered fields correspond to the same geometry, greatly increasing the value of the comparison.

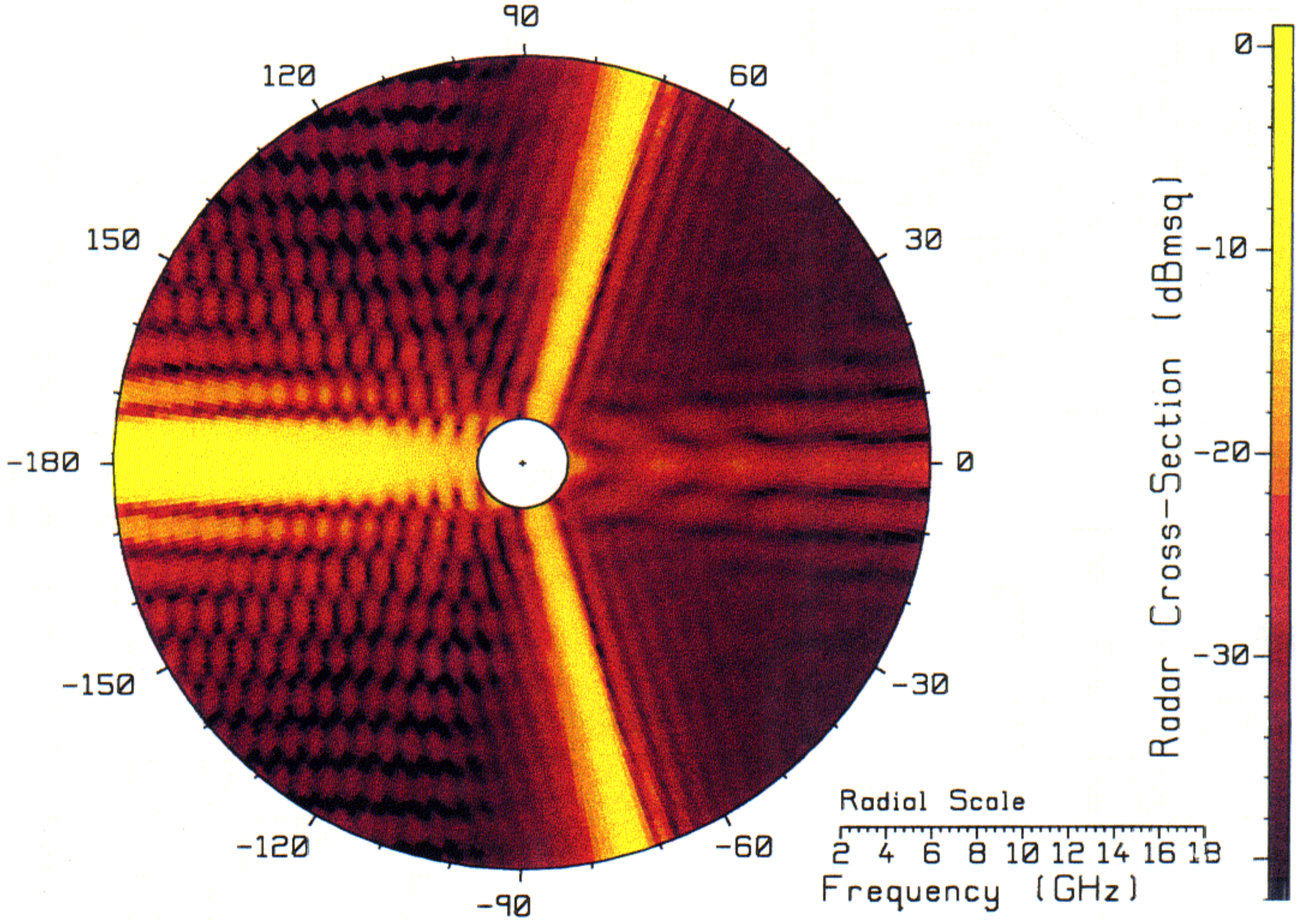

Fig. 5 The RCS of the large cone of Fig. 2(c) for horizontal polarization. outer circle.

### 1.3 Six Targets

Fig. 2 shows the set of six targets which will be discussed in this paper. Table 1 lists the range $R$ and bistatic angle $\alpha$ used in the measurement of the scattered field for each target. In all cases the horn separation is 17.46 cm, and the bistatic angle is $\alpha = 2\tan^{-1}(h/(2R))$. The measured data in this paper was taken from 2 to 18 GHz. Table 1 lists the maximum frequency from Eqn. (4) at which the "rule-of-thumb" of Eqn. (3) is satisfied. The measured data for the strip, the cone-sphere, the thick disk and the small cone targets satisfy Eqn. (3) to beyond 18 GHz, but for the large rod and the large cone the range is too short.

Fig. 2 shows the shapes and relative sizes of the targets which will be studied in this paper. The figure shows two views of each target, in an *xy* plane at the top, and in an *xz* plane at the bottom. All six targets in Fig. 2 are metallic. The targets are: (a) a thin strip, of length 10 times its height; (b) a large rod of square cross-section; (c) a large right-circular cone; (d) a small cone-sphere; (e) a thick disk; and (f) a small cone. Table 1 gives the dimensions of each target. Fig. 2 shows the orientation of each target relative to the *xyz* coordinate system corresponding to the measurement setup in Fig. 1. In Table 1, "vertical polarization" has the electric field vector parallel to the $z$ axis, and "horizontal polarization" has the electric field in a plane parallel to the *xy* plane.

### 1.4 Polar Color Maps

Figs. 3 to 8 show "polar color maps" of the RCS of each target in dB relative to the square metre. The angle axis corresponds to the angle of incidence $\theta$ on the target, with the $x$ direction oriented toward the right and the $y$ direction pointing upward. Radial distance from the center of the graph is proportional to the frequency $f$. To preserve the geometric relationships discussed later in this paper, the center of the polar axes must correspond to zero frequency.

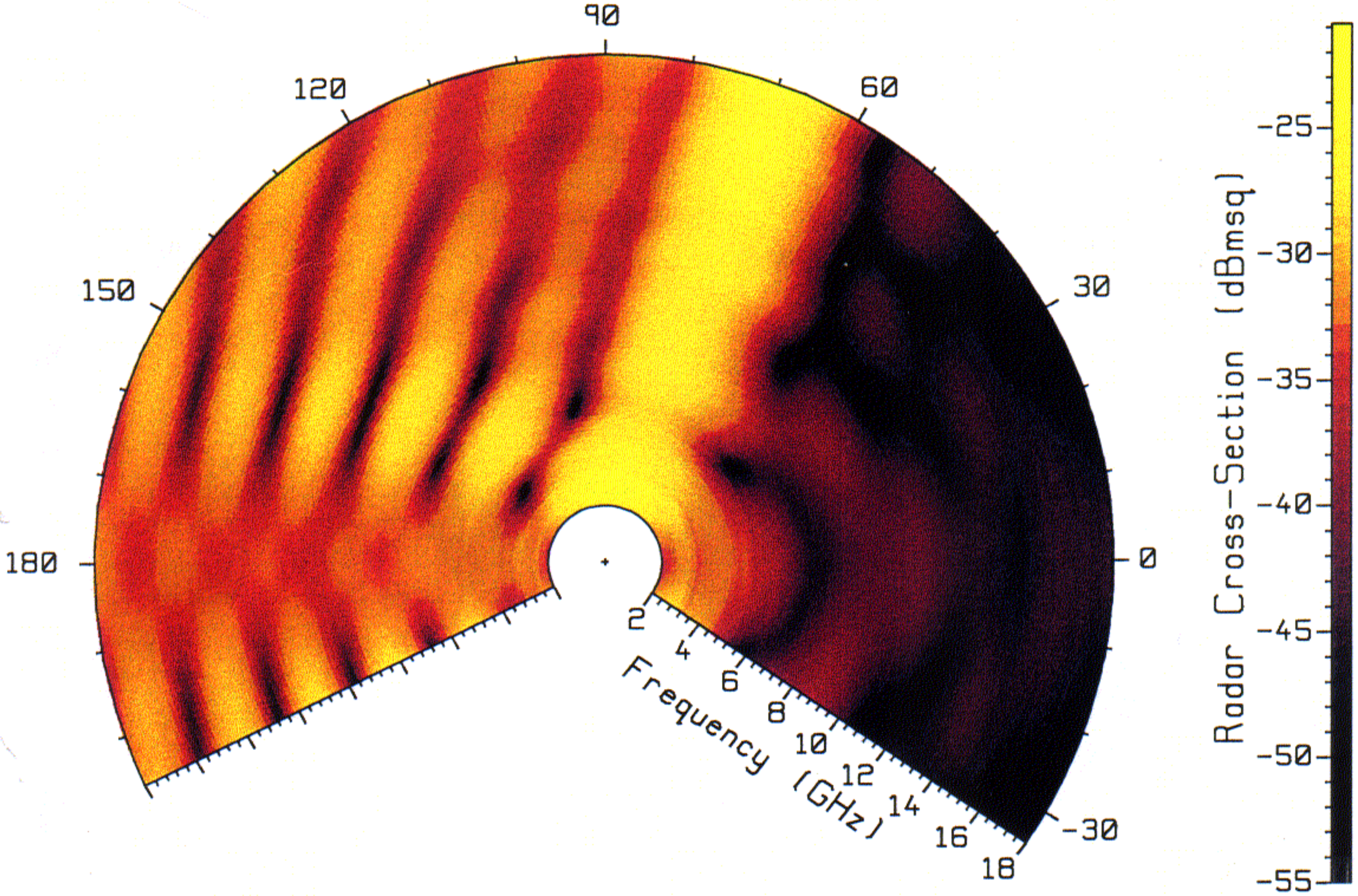

Fig. 6 The RCS of the cone-sphere of Fig. 2(d) for horizontal polarization.

In the polar axes in Figs. 3 to 8, the inner circle corresponds to 2 GHz, and the frequency increases linearly with radius to 18 GHz on the outer circle. Each point $(f,\theta)$ between the inner and outer circle represents a unique frequency and incidence angle. The rectangular coordinates of point $(f,\theta)$ will be denoted using $(u,v)$, where $u = f\cos\theta$ and $v = f\sin\theta$ have the units of frequency.

The RCS could be graphed as a conventional contour map using solid lines to show RCS contours at specified levels, say 3 dB apart. Contour lines can be drawn in color, with colors corresponding systematically to levels of RCS contours, making the regions of high and of low RCS easier to distinguish. By filling the regions between contours with color, we obtain a "color contour map", which reveals patterns in the RCS more boldly than do simple contour lines. Such a map is constructed by assigning a color to each range of RCS $\sigma$; thus color #$k$ is used to plot RCS values in a range $\sigma_{k-1} \le \sigma < \sigma_k$. Various color scales were discussed in Ref. [8]. The RCS at each pixel location is interpolated from the measured data near that frequency and incidence angle, then each pixel is assigned a color according to the RCS value. If only 16 colors are used, then the changes in color are clearly seen as curves of constant RCS at levels $\sigma_k$. When the number of colors is increased to about 200, the color appears to vary continuously, as shown in Figs. 3 to 8. These figures were made using program POLPLOT, which was written to display RCS and other data in the polar color map format. POLPLOT for Microsoft Windows is available from the authors at no charge.

Figures 3 to 8 show some remarkable geometric patterns. Figs. 3, 4, and 7 show distinct straight bands of maximum and minimum RCS. Figs. 4 and 5 show sets of dark bands, delineating a pattern of bright dots. Fig. 6 shows hyperbolas. Figs. 7(b) and 8 show parts of ellipses. In the following we will identify simple scattering mechanisms that give rise to these features. To understand the patterns

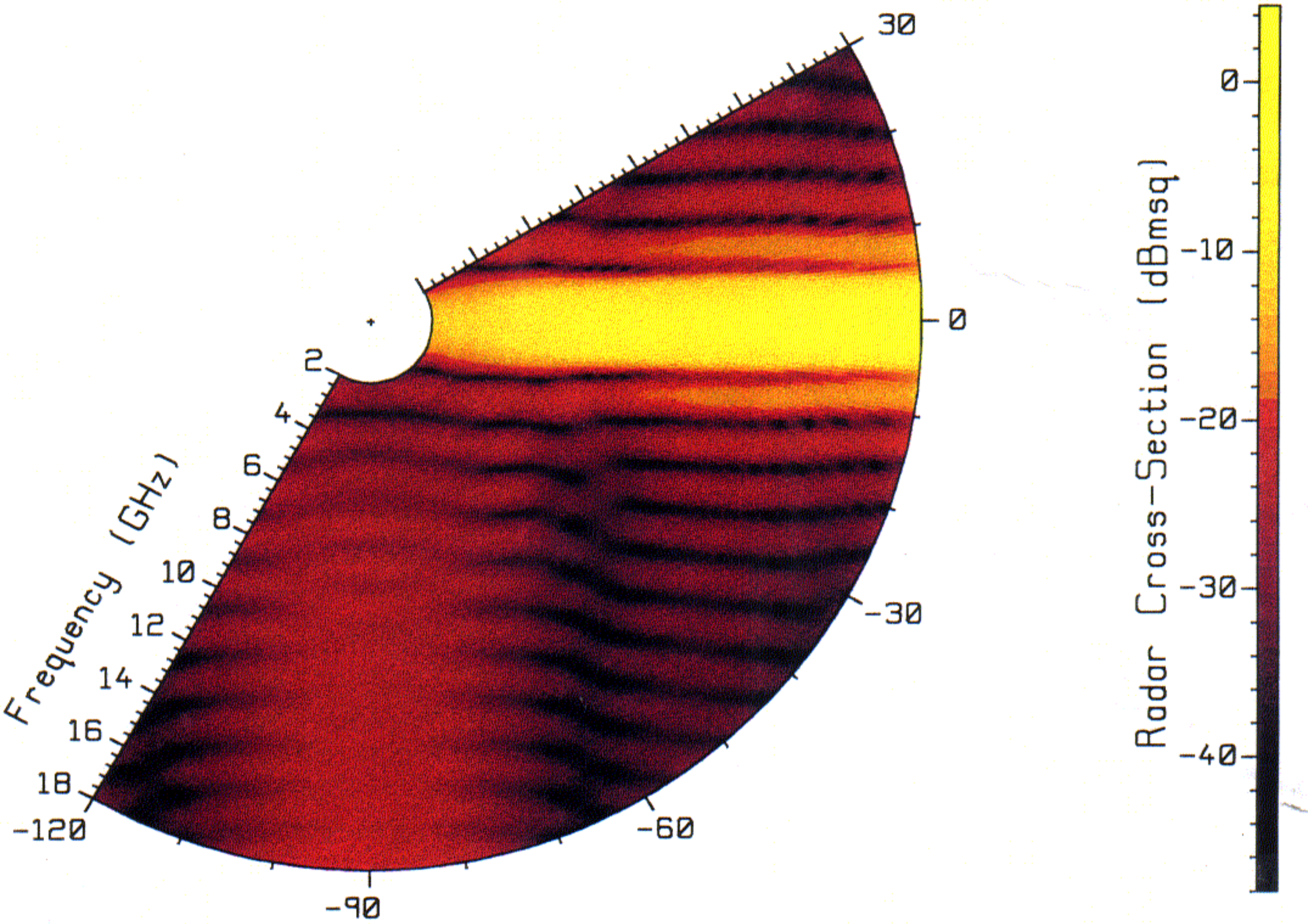

Fig. 7(a) The RCS of the thick disk of Fig. 2(e) for horizontal polarization.

seen in the figures, and associate them with target scattering mechanisms, it will be sufficient to assess the backscattered field due to an incident plane wave, rather than analyze the more complex measurement geometry of Fig. 1.

## 2. INTERFERENCE OF POINT SOURCES

Many of the targets of Fig. 2 scatter by diffraction from points on edges or from tips. This section shows that interference of the scattered fields from two point sources leads to a set of parallel lines of maximum and minimum RCS on a contour map in polar format.

Fig. 9 shows a plane wave traveling parallel to the $xy$ plane in direction $\theta$ to the $x$ axis. The plane wave scatters from two diffraction points, such as points on edges. In Fig. 9, the diffraction points are located on the $x$ axis, separated by distance $d$. The observer is at a distant point in the $xy$ plane in the backscatter direction. The round trip path length from the observer to point #1 and back to the observer is $L_1$, and that to and from point #2 is $L_2$. The difference between the path lengths is

$$L_2 - L_1 = 2d\cos\theta \qquad \text{...(5)}$$

Let $\alpha_1$ and $\alpha_2$ be the phase changes associated with the diffraction process at source #1 and source #2, respectively. Then if the plane wave has zero phase at the observer, the phase of the diffracted field due to source #1 is $\alpha_1 - kL_1$, and to source #2, $\alpha_2 - kL_2$, where $k = 2\pi f / c$ is the wave number and $c$ is the speed of light. There will be an RCS maximum when the phase difference between the diffracted fields at the observer is $-2\pi n$, where $n$ is an integer, positive, zero, or negative. Thus there will be an RCS maximum when

$$-k(L_2 - L_1) + (\alpha_2 - \alpha_1) = -2\pi n \qquad \text{...(6)}$$

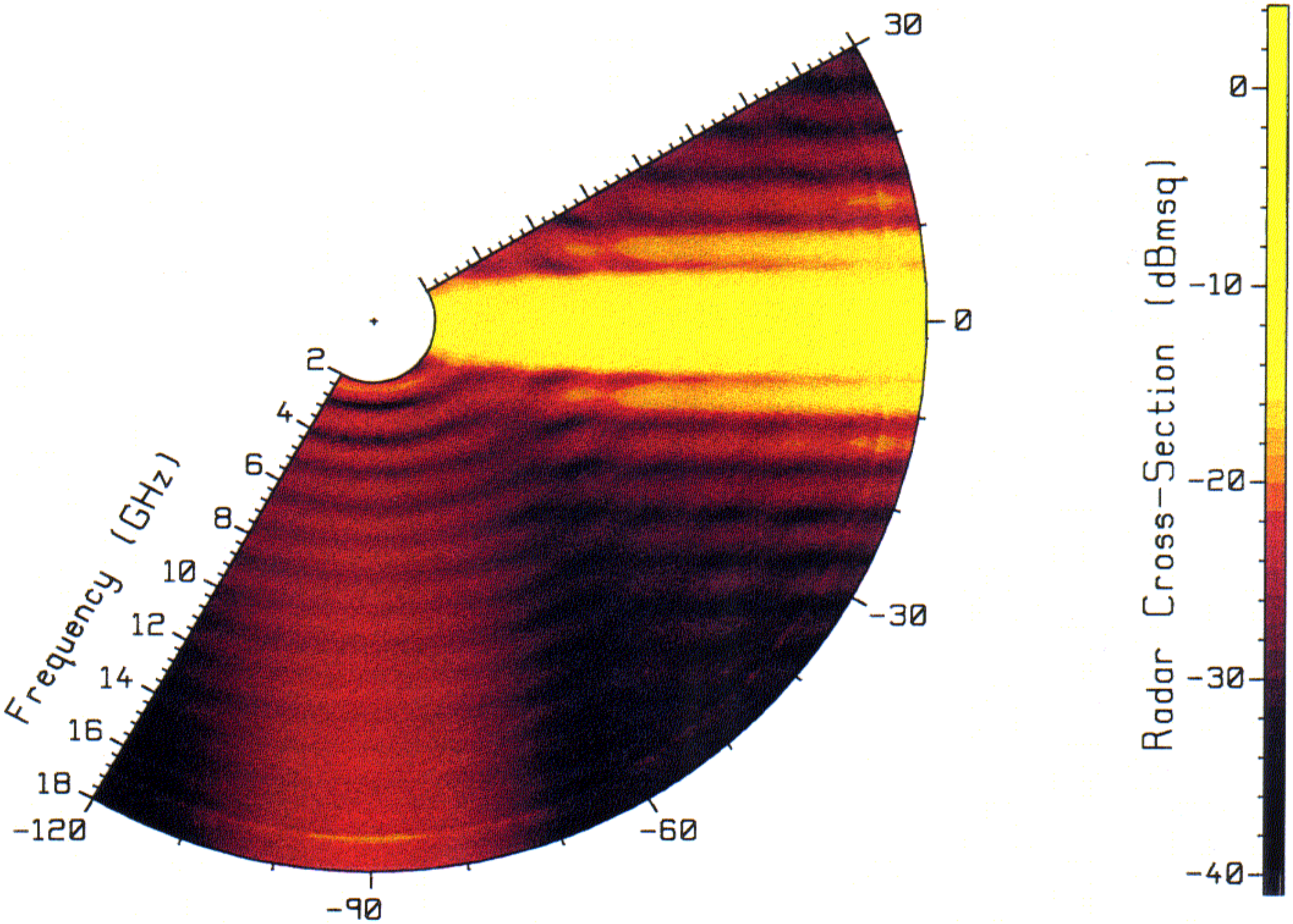

Fig. 7(b) The RCS of the thick disk of Fig. 2(e) for vertical polarization.

Equations. (5) and (6) can be rearranged to show that contours of maximum RCS satisfy

$$f\cos\theta = \frac{c}{2d}\left(n+\frac{\alpha_2-\alpha_1}{2\pi}\right) \qquad \ldots(7)$$

The results presented in the following indicate that the phase changes associated with the diffraction process, $\alpha_1$ and $\alpha_2$, are reasonably constant with frequency and incidence angle. If *(u,v)* gives the location of a point on a polar contour map, then $u = f\cos\theta$, and Eqn. (7) states that the curves of maximum RCS have constant *u*, that is, are straight lines parallel to the *v* axis. The lines of maximum RCS are at positions

$$u_n = \frac{c}{2d}\left(n+\frac{\alpha_2-\alpha_1}{2\pi}\right) \qquad \ldots(8)$$

The spacing of these lines is given by

$$\Delta u = u_{n+1} - u_n = \frac{c}{2d} \qquad \ldots(9)$$

Note that curves of minimum RCS satisfy Eqn. (6) with the right-hand side replaced by $-2\pi n - \pi$, hence lead to vertical straight lines with the same spacing as the lines of maximum RCS. The spacing of these lines of minimum or maximum RCS provides a convenient comparison with the measured data because it is independent of $\alpha_1$ and $\alpha_2$. The following demonstrates lines of maximum and minimum RCS for the strip, the large rod, and the right circular cone.

## 2.1 The Thin Strip

The thin metallic strip of Fig. 2(a) has length 63.6 mm, width 6.36 mm, and thickness 0.32 mm. The strip lies in the *xz* plane with the long dimension parallel to the *x* axis. The RCS was measured with the incident electric field

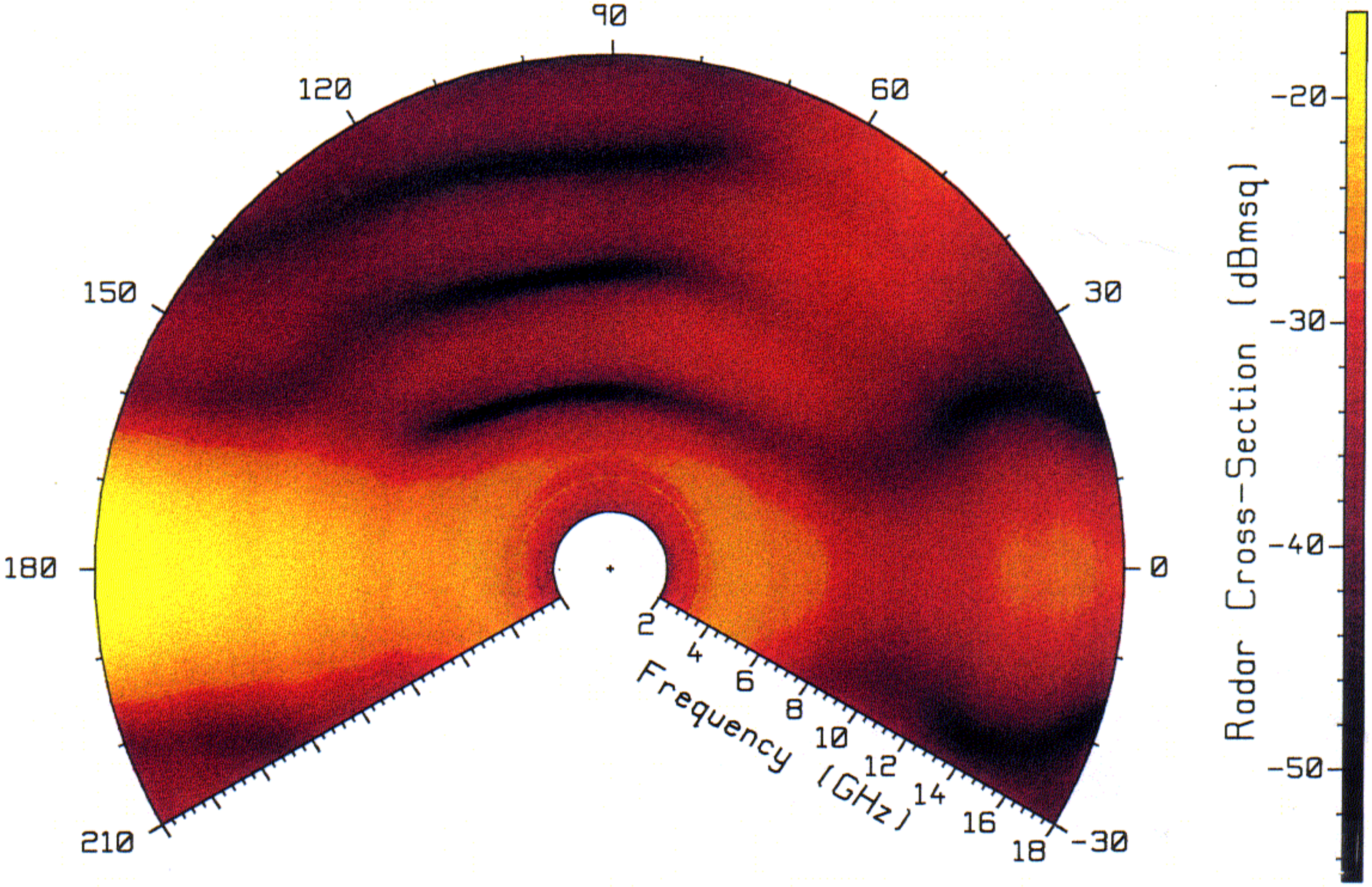

Fig. 8 The RCS of the small cone of Fig. 2(f) for vertical polarization.

parallel to the $z$ axis, that is, with "vertical polarization". The RCS was measured from 2 to 18 GHz, for angles of incidence from $\theta = 0$ or "end-on" through $\theta = 90$ or "broadside", all the way around back to $\theta = 0$, to obtain the polar color map of Fig. 3. The maxima in the RCS show a striking pattern of bright vertical bands, separated by dark bands of minimum RCS. For end-on incidence, the frequencies at which the maxima fall in Fig. 3 can be read from their intersections with the horizontal axis, to obtain 3.4, 5.8, 8.2, 10.6, 13.0 and 15.4 GHz, spaced 2.4 GHz apart. The largest maximum in Fig. 3 falls on the vertical axis, for $\theta = 90$ degrees or "broadside" incidence, and is due to specular reflection from the face of the strip.

The bands in Fig. 3 are readily explained by ignoring the thickness of the strip, and considering interference between the fields diffracted from the two ends of the strip. For a plane wave incident in the $xy$ plane and an observer located at any finite distance in the backscatter direction, there is only one point on the leading edge of the strip and only one point on the trailing edge that satisfy the law of diffraction[9]. The scattering geometry is that of Fig. 9 with $d$=63.6 mm, so we expect the maxima in the RCS to fall along vertical lines spaced according to Eqn. (9) by $c/(2d)$=2.36 GHz, close to the 2.4 GHz spacing seen in Fig. 3.

We can estimate the phase change associated with diffraction at the leading end and trailing end of the strip using the wedge diffraction coefficients given in Ref. [9]. Thus considering the ends of the strip to be wedges of angle zero degrees, we can evaluate the phase of the soft diffraction coefficient $D_s$, for backscatter with the angle of incidence equal to the angle of diffraction. For the leading end we obtain $\alpha_1 = 3\pi/4$ and for the trailing end $\alpha_2 = -\pi/4$, and so $\alpha_2 - \alpha_1 = -\pi$. Evaluating Eqn. (8) with $d$=63.6 mm obtains maxima at 1.2, 3.5, 5.9, 8.3, 10.6, 13.0, 15.3 and 17.7 GHz, quite close to the values of 3.4, 5.8, 8.2, 10.6, 13.0 and 15.4 GHz, read from Fig. 3.

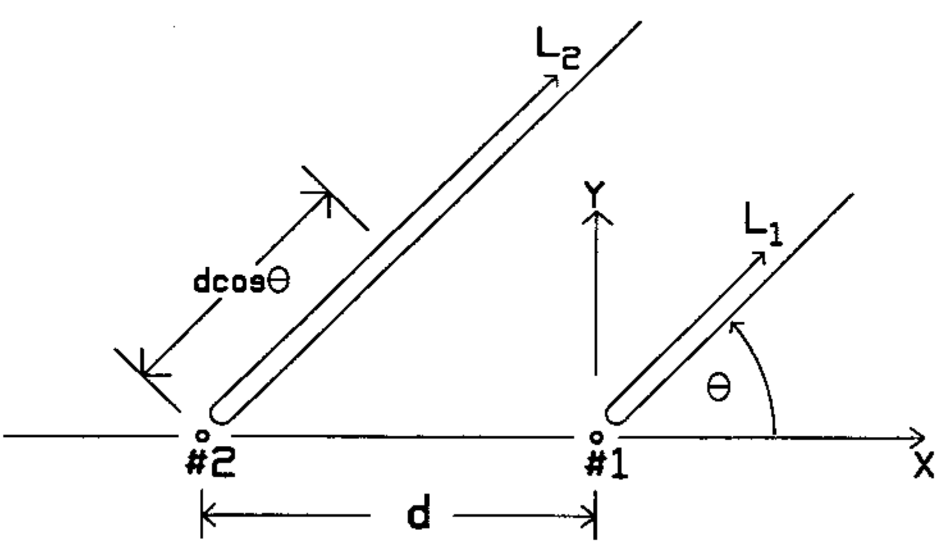

Fig. 9 Two scattering points separated by distance $d$, showing the path lengths $L_1$ and $L_2$.

If there were no specular reflection, we would expect to see bands of maximum RCS in Fig. 3 intersecting the horizontal axis at $u = \pm 1.2$ GHz, separated by a minimum at $u$=0 on the vertical axis. Specular reflection merges these two bands into a single wide band centered on the vertical axis. It is interesting to note in Fig. 3 that this bright band of specular reflection has a constant width as distance from the center of the graph increases, that is, as the frequency $f$ increases. This is consistent with the fact that the angular width $\Delta\theta$ of a lobe due to specular reflection is inversely proportional to the frequency[9], $\Delta\theta \propto 1/f$. The arc width of the reflection on the polar map, $\Delta s = f\Delta\theta$, becomes constant when $\Delta\theta$ is proportional to $1/f$, and this is clearly seen in Fig. 3.

## 2.2 The Large Rod

Fig. 2(b) shows a metallic rod of length 177.8 mm and square cross-section of size 71.1 mm. The rod is oriented with its edges parallel to the coordinate axes, and the long axis parallel to the $x$ direction. The RCS was measured with the incident electric field horizontally polarized, that is, with the electric field vector parallel to the $xy$ plane in Fig. 2. Fig. 4 shows the polar color map of the RCS of the rod in the first quadrant. We see a pattern of vertical dark bands of minimum RCS intersecting a pattern of horizontal dark bands, with the vertical bands more closely spaced than the horizontal. There is a third set of parallel dark bands oriented obliquely. The three sets of dark bands define a pattern of bright dots of maximum RCS. The spacing of the bands can be read directly from the color map with the aid of a ruler, dividers, and a calculator. The vertical bands are spaced by 0.842 GHz, the horizontal bands by 2.00 GHz, and the oblique bands by 0.776 GHz.

We can understand the scattered field of the rod as arising from diffraction from the three $z$-directed edges exposed to the plane wave for any direction of incidence. The diffraction points on two adjacent edges spaced by the length of the rod lead to a set of equally-spaced dark vertical bands of minimum RCS on the polar color map, with the expected spacing given by $c/2d$ = 300/(2 x 177.8)= 0.844 GHz, close to the value of 0.842 GHz read from Fig. 4. The two adjacent edges spaced by the width of the rod give rise to a set of dark bands of RCS parallel to the horizontal axis, spaced by $c/2d$=300/(2 x 71.1)=2.11 GHz. The third pair of edges are diagonally opposite one another, and are spaced by 191.5 mm. These produce the oblique set of bands, spaced by $c/2d$=300/(2 x 191.5)=0.783 GHz, close to the value of 0.776 GHz seen in Fig. 4. The tilt of this set of bands is expected to be at an angle of $\tan^{-1}(177.8/71.1) = 68$ degrees to the horizontal, and agrees quite well with the color map. The bright dots in the pattern have the same relative proportions as the target.

## 2.3 The Cone for Horizontal Polarization

The cone of Fig. 2(c) has a half angle of 15.26 degrees and the diameter of the base is 80.5 mm. The long axis of the cone lies along the $x$ axis, with the tip pointing in the $+x$ direction. The cone length from the tip to the center of the base is 147.6 mm, and the "side length" from the tip to the edge of the base is 153.0 mm. The RCS was measured with horizontal polarization from 2 to 18 GHz over a full 360 degrees and is plotted as a polar color map in Fig. 5. The figure shows a maximum return for $\theta = 180$ degrees, due to specular reflection when the plane wave is normally incident on the flat base of the cone. The RCS is also large

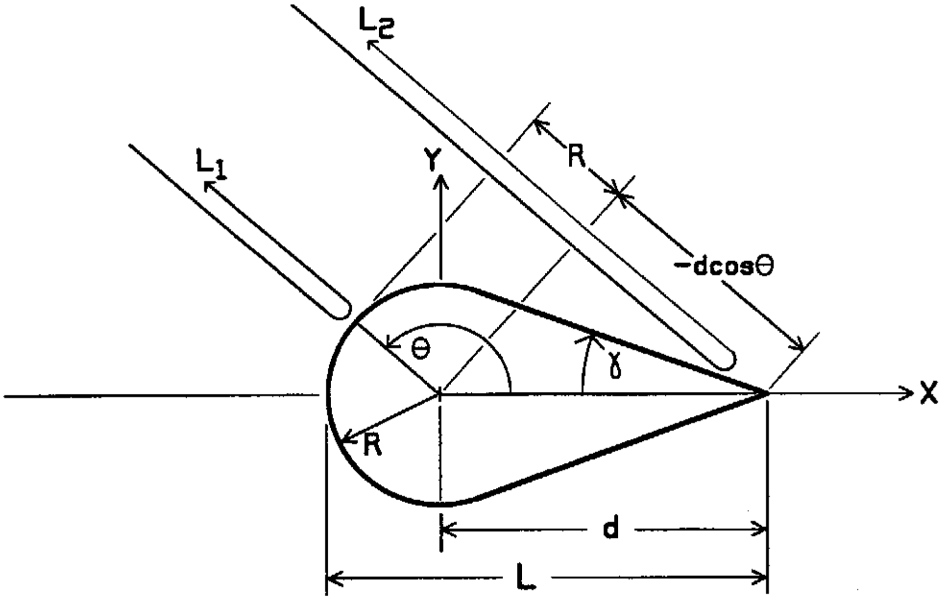

Fig. 10 The cone-sphere, showing the path lengths $L_1$ and $L_2$ for an incidence angle in the second quadrant.

along the bands oriented at ±7.5 degrees to the positive *x* axis, looking perpendicular to the surface of the cone.

For incidence angles near zero degrees, the color map of Fig. 5 shows a pattern of horizontal bands of maximum and minimum RCS. This arises from the interference of the edge-diffracted fields from two diametrically-opposite points on the edge of the base. The two diffraction points lie in the *xy* plane in the coordinates of Fig. 2, and are separated by 80.5 mm, hence we expect the maxima or the minima to be spaced by $c/2d$=300/(2 x 80.5)=1.86 GHz. The spacing of the minima near 0 degrees in Fig. 5 can be read from the color map as roughly 1.7 GHz, reasonably consistent with the expected value. For incidence angles greater than 15 degrees, the incident plane wave no longer "sees" the point on the cone base in the -*y* half-space, and the set of bands fades away.

At 75 degrees incidence, the direction of travel of the plane wave is normal to the surface of the cone and there is a strong specular return. For angles between about 50 and 90 degrees, Fig. 5 shows a set of parallel bands of maximum RCS, parallel to the strong return at 75 degrees. From these incidence angles there is interference in the backscatter direction between the diffracted field from the nearest point on the edge of the base and the diffracted field from the tip. These points are separated by the cone's side length of 153 mm and so we expect the minima to be spaced by $c/2d$ = 300/(2 x 153)=0.98 GHz. A ruler and dividers can be used to estimate the spacing of these minima in Fig. 5 as about 1.03 GHz, consistent with our expectations.

For incidence angles between 90 and 165 degrees, the incident plane wave sees the tip plus the two diffraction points on the edge of the base. These three scattering points lead to three sets of intersecting dark bands of minimum RCS. Diffraction from the two points on the edge gives rise to a continuation of the set of horizontal bands spaced by 1.86 GHz that is seen between 0 and 15 degrees incidence. There are two pairs consisting of the tip plus one of the two diffraction points on the edge. Diffraction from the tip plus the scattering point on the edge in the +*y* half-space gives rise to a set of parallel bands tilted at an angle of about 15 degrees from the vertical direction toward the positive horizontal axis in the color map. This set of dark bands is parallel to the direction of the large return at about 75 degrees and is clearly seen in the 90 to 165 degree angular sector. The tip plus the diffraction point on the base in the -*y* half-space produces a set of parallel bands inclined at 15 degrees from the vertical direction toward the negative horizontal axis, and is also clearly seen in the color map. The spacing of the oblique bands can be read from Fig. 5 as about 1 GHz, close to the expected value of 0.98 GHz. The three sets of intersecting dark bands in Fig. 5 define a pattern of bright dots of maximum RCS similar to that of the rod in Fig. 4. For incidence angles between 165 and 195 degrees, the tip is not seen, as it lies in the shadow of the base. The dot pattern is replaced by the pattern of horizontal bands associated with scattering from the two diffraction points on the edge.

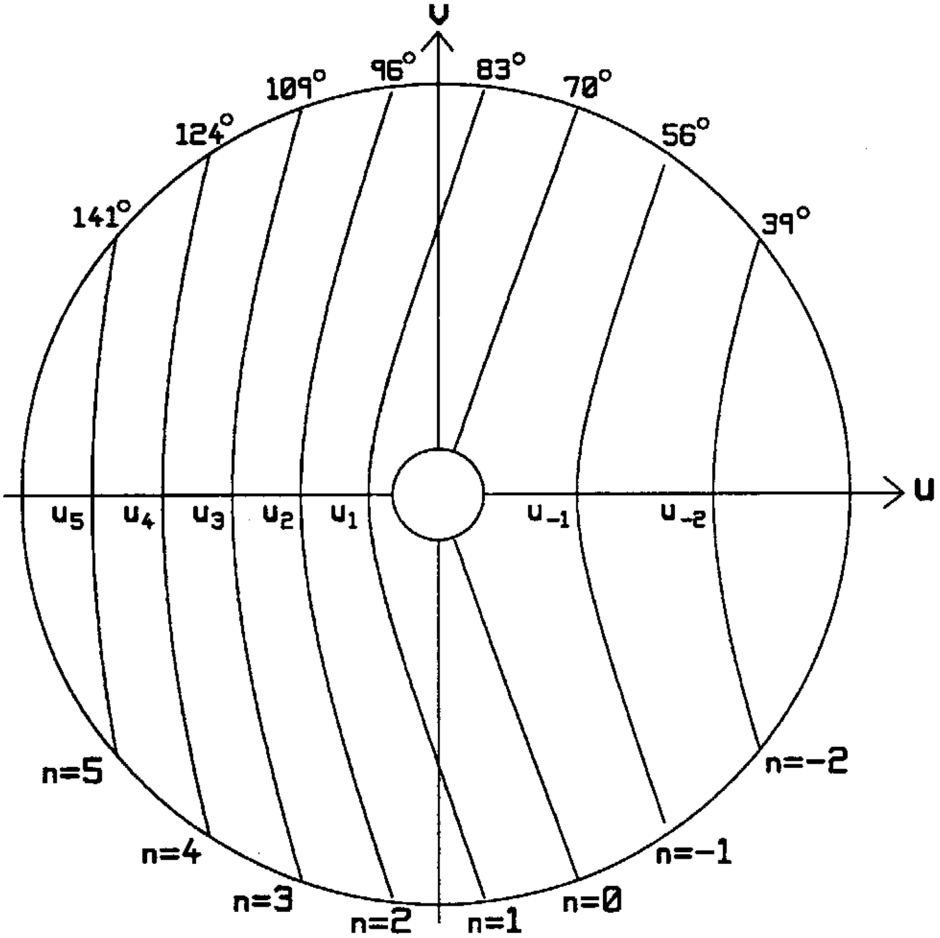

Fig. 11 Hyperbolas of minimum RCS for the cone-sphere.

## 3. INTERFERENCE OF A SPHERE REFLECTION AND A TIP DIFFRACTION

The cone-sphere of Fig. 10 illustrates interference between reflection from the spherical endcap and diffraction from the tip. The cone-sphere is oriented with its axis along the $x$-axis. There is no edge at the junction of the cone and the spherical endcap, that is, the unit-normal to the surface is continuous in passing from the surface of the cone to the surface of the sphere. In Fig. 10, a plane wave incident on the cone-sphere in the angular range $(90-\gamma)<\theta$ $<(180-\gamma)$ sees both the surface of the sphere and the tip of the cone. The difference between the round-trip distance $L_1$ from the observer to the sphere back to the observer, and $L_2$ from the observer to the tip and back, is

$$L_2-L_1=2(R-d\cos\theta) \qquad \ldots(10)$$

The curves of minimum RCS satisfy

$$-k(L_2-L_1)+(\alpha_2-\alpha_1)=-\pi-2\pi n \qquad \ldots(11)$$

hence the RCS is a minimum when

$$f=\frac{c}{2(R-d\cos\theta)}\left(n+\frac{\pi+\alpha_2-\alpha_1}{2\pi}\right) \qquad \ldots(12)$$

where $\alpha_1$ is the phase change associated with the reflection from the surface of the sphere, and $\alpha_2$ with the diffraction process at the tip of the cone. Eqn. (12) defines a set of hyperbolas[13] having their major axes aligned with the horizontal axis, such as those shown in Fig. 11. It may be shown that the crossing points of the hyperbolas with the negative horizontal axis are given by

$$u_n=-\frac{c}{2(d+R)}\left(n+\frac{\pi+\alpha_2-\alpha_1}{2\pi}\right) \qquad \ldots(13)$$

Hence the crossings of the negative $u$ axis are evenly spaced with the spacing given by

$$\Delta u = \frac{c}{2(d+R)} \qquad \ldots(14)$$

The spacing of the crossing points provides a convenient comparison with the measured RCS.

### 3.1 The Cone-Sphere

The metallic cone-sphere of Fig. 2(d) has a half-angle of $\gamma = 19.7$ degrees, and an overall length of $L$=50.1 mm. The diameter of the sphere is 25.3 mm. The distance from the center of the sphere to the tip of the cone is $d$=37.45 mm. The RCS was measured with horizontal polarization from 2 to 18 GHz over an angular range from -30 to 210 degrees as shown in Fig. 6. The map shows a strong reflection at an incidence angle of 70 degrees, looking normal to the cone surface. Also there is strong reflection from about 160 to 200 degrees, looking normal to the surface of the sphere, over the angular range where the tip of the cone is not visible. In the left-hand plane in Fig. 6 there is a set of five sharp bands of minimum RCS, separated by broad regions of large RCS.

Fig. 11 shows the set of hyperbolas of minimum RCS specified by Eqn. (12) for the cone-sphere dimensions of $R$= 12.65 mm and $d$=37.45 mm. In Fig. 11 the radial axis corresponds to Fig. 6, with zero frequency at the center, 2 GHz at the inner circle, and 18 GHz at the outer. We expect the reflection from the sphere surface to have a phase change of $\alpha_1 = \pi$. The phase change associated with the tip diffraction is more difficult to estimate, and was simply made equal to zero, $\alpha_2 = 0$. Comparing Figs. 6 and 11 we see that the dark bands of minimum RCS in Fig. 6 have the same shape as the hyperbolas of Fig. 11. There are five hyperbolas in Fig. 6, and five in Fig. 11, in the negative-$u$ half-space. In Fig. 6, only segments of the hyperbolas are seen. For $\theta < 70$ degrees the surface of the cone hides the surface of the sphere, and so there is no reflection and the hyperbolas are not formed. From $\theta = 160$ to 200 degrees, the tip of the cone is not visible and so the segments of the hyperbolas that cross the horizontal axis are not seen. By smoothly joining the portions of the hyperbolas in the negative half-space with those in the positive, we can estimate the spacing of the zero crossings as about 2.9 GHz, in reasonable agreement with the spacing of 3.0 GHz predicted by Eqn. (14).

Another comparison of the position of the hyperbolas in Figs. 6 and 11 can be made by reading the angles at which they cross the 18 GHz circle. Thus in Fig. 6, the minima in the RCS at 18 GHz occur at about 82, 93, 106, 120 and 138 degrees. In Fig. 11, these crossings fall at 83, 96, 109, 124 and 141 degrees. The alignment of the hyperbolas predicted by our simple interference theory with those in the measured RCS is quite good, especially considering that the phase change $\alpha_2$ associated with diffraction at the tip of the cone was simply set to zero. If we use $\alpha_2 = -45$ degrees, then the minima at 18 GHz fall at 82, 95, 108, 122 and 138 degrees, in better agreement with the measurement, and so the phase change associated with tip diffraction must be closer to -45 degrees than to 0 degrees.

## 4. INTERFERENCE OF AN EDGE WAVE AND AN EDGE DIFFRACTION

To analyze the polar color maps of scattering from the thick disk and the small cone of Fig. 2 parts (e) and (f), it is useful to consider a wave which travels around the edge of the target, called an "edge wave"[14]. Fig. 12 shows a thin disk in the $yz$ plane, with a plane wave incident nearly edge-on to the disk. The wave diffracts from the nearest point on the disk edge, with path length $L_1$. The wave also diffracts from the disk edge at a point diametrically opposite, but the path is not shown in Fig. 12. In addition, the wave couples to the edge of the disk and becomes an "edge wave", which travels around the edge, shedding energy tangentially as it goes. After traveling a distance of $\pi R$ around the edge, the edge wave launches some of its energy in the backscatter direction. We will show that interference between the two scattered fields shown in Fig. 12 creates a pattern of ellipses.

### 4.1 Interference Analysis

Fig. 12 compares the path lengths $L_1$ traveled by the wave diffracted from the edge of the disk, and $L_2$ traveled by the wave that couples to the edge and follows it around a semicircle. For $0 \le \theta \le 180$ degrees, the difference in path length is

$$L_2 - L_1 = \pi R + 2R\sin\theta \qquad \ldots(15)$$

Assuming the wave travels around the edge with the same phase constant as in free space, these waves will be 180 degrees out of phase in the backscatter direction when Eqn. (15) is satisfied, leading to curves of minimum RCS which satisfy

$$f = \frac{c}{(\pi + 2\sin\theta)R}\left(n + \frac{\pi + \alpha_2 - \alpha_1}{2\pi}\right) \qquad \ldots(16)$$

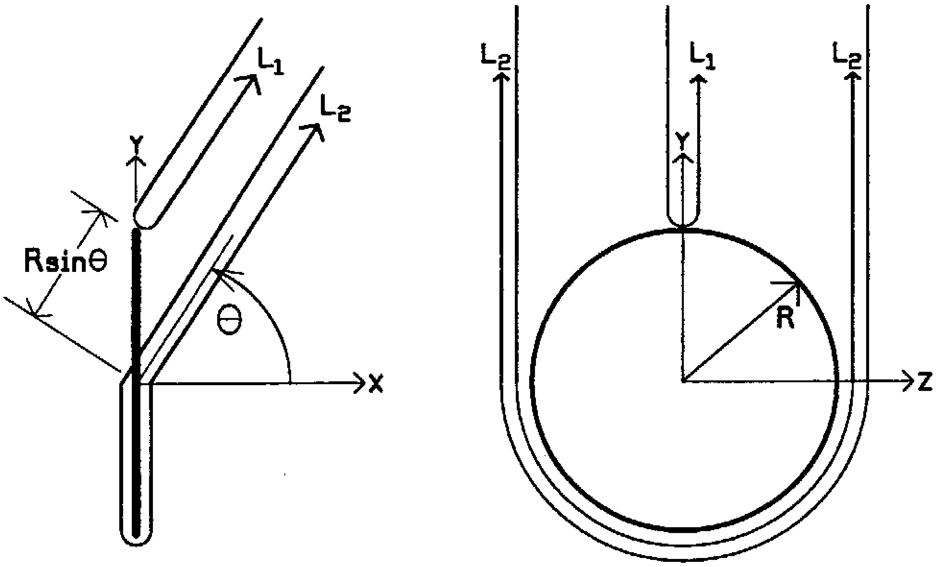

Fig. 12 A thin disk, showing diffraction from the edge with path length $L_1$, and scattering by an edge wave which travels around the edge of the disk, with path length $L_2$.

where $n$=0, +-1, +-2, .... Angles $\alpha_1$ and $\alpha_2$ are phase changes associated with the scattering process for the edge-diffracted wave and for the wave that travels around the edge. For $180 < \theta < 360$ degrees, we must use the diffraction point diametrically opposite on the edge, hence $L_2 - L_1 = \pi R - 2R\sin\theta$, and the curves of minimum RCS satisfy

$$f = \frac{c}{(\pi - 2\sin\theta)R}\left(n + \frac{\pi + \alpha_2 - \alpha_1}{2\pi}\right) \qquad \ldots(17)$$

Equations (16) and (17) can generate both positive and negative frequencies, depending on the values of $n$, $\alpha_1$ and $\alpha_2$, but only the positive frequencies are physically meaningful.

Each of Equations (16) and (17) represents a family of ellipses, with the major axis aligned along the vertical axis and one focus at the origin[13]. To illustrate interference ellipses that arise due to the edge wave, these equations were graphed using the radius of the base of the small cone of Fig. 2(f), $R$=29.8/2=14.9 mm, and using $\alpha_1 = 135$ degrees, and $\alpha_2 = -136$ degrees as explained below. The set of ellipses so obtained is shown in Fig. 13. Eqn. (16) leads to positive and negative frequencies depending on $n$ and on $\alpha_2 - \alpha_1$; only those ellipses having positive frequencies are graphed in Fig. 13. The ellipses of Eqn. (16) were drawn using solid curves in the upper half-space where Eqn. (15) holds; dashed curves were used in the lower half-space to show the orientation of the major axis. Eqn. (17) leads to the set of ellipses shown with solid curves in the lower half-space in Fig. 13.

In Fig. 13, the points at which the ellipses cross the vertical axis have been labeled $v_1$, $v_2$, and so forth. Eqn. (16) is easily evaluated with $\theta = 90$ degrees to show that if $\alpha_1$ and $\alpha_2$ are independent of the frequency, then the spacing of the crossing points is uniform and is given by

$$\Delta v = v_{n+1} - v_n = \frac{c}{(\pi + 2)R} \qquad \ldots(18)$$

The thick disk of Fig. 2(e) and the cone of Fig. 2(f), with its circular-disk base, will be used to illustrate ellipses in RCS polar color maps.

### 4.2 The Thick Disk

The disk of Fig. 2(e) demonstrates the edge wave for vertical polarization, and its absence for horizontal polarization. The disk is metallic, of radius $R$=50.45 mm and thickness 20.4 mm. The disk was oriented so that its flat faces lie parallel to the $yz$ plane. The RCS was measured for both horizontal polarization, Fig. 7(a), and vertical polarization, Fig. 7(b), from 2 to 18 GHz. There are strong similarities between the two cases. In both cases specular reflection from the face of the disk obtains a very strong RCS at $\theta = 0$ degrees. In both parts of Fig. 7 there is a set of bands of maximum and of minimum RCS parallel to the horizontal axis near $\theta = 0$ degrees. But near $\theta = -90$ degrees, which is edge-on incidence to the

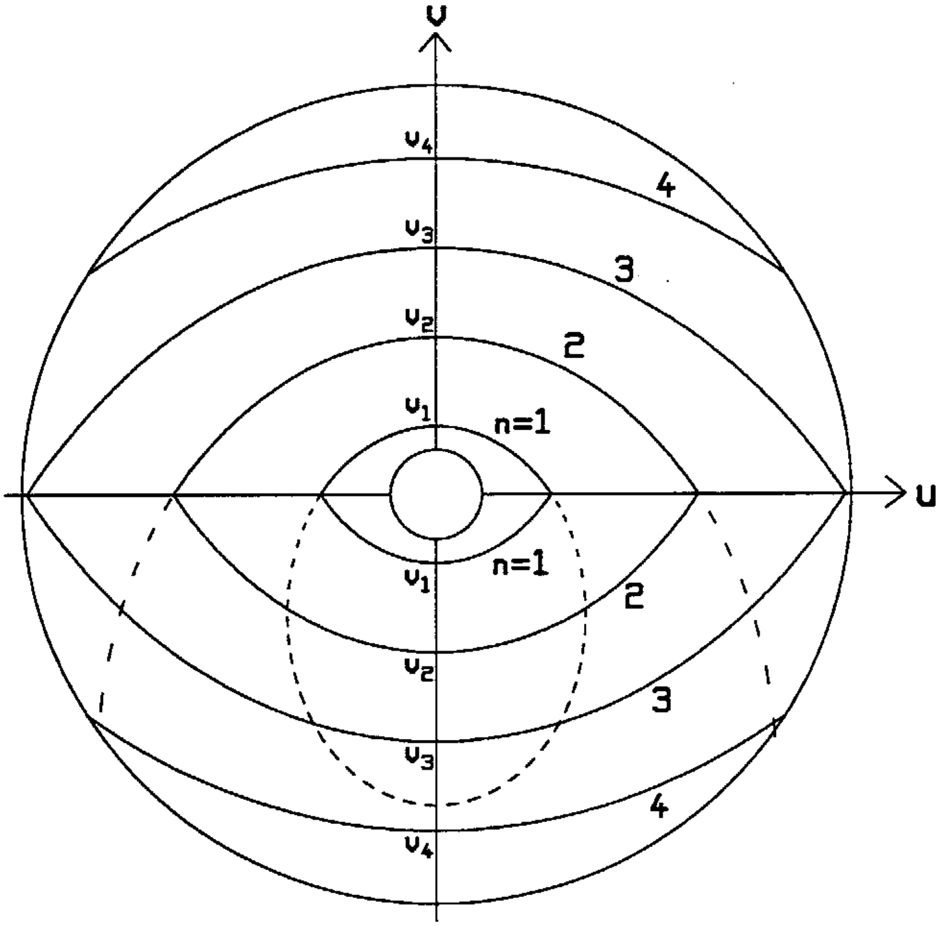

Fig. 13 Ellipses of minimum RCS for the small cone.

disk, the two cases are significantly different. For horizontal polarization the pattern of parallel straight bands continues from $\theta = 0$ to $\theta = -90$ degrees. However, for vertical polarization, part (b), the set of maxima and minima near $\theta = -90$ degrees have substantial curvature. These appear to be segments of ellipses.

The set of horizontal bands near $\theta = 0$ degrees for both polarizations arise due to diffraction from two diametrically-opposite points on the edge of the disk, where the disk intersects the *xy* plane. These points are spaced by the disk diameter of $d$=2$R$=100.9 mm, and Eqn. (9) predicts the band spacing to be $c/(2d)$=300/(2 x 100.9)= 1.49 GHz. For horizontal polarization in Fig. 7(a), the spacing can be read from the figure as 1.46 GHz, close to the expected value. For horizontal polarization, this pattern of horizontal bands continues with the same spacing throughout the whole color map. The pattern is clearly seen along the $\theta = -90$ degrees direction from 2 to about 9 GHz, but the RCS tends to become flat for $\theta = -90$ above 9 GHz. Note that there are two vertically-oriented dark bands, at 7.5 and 15 GHz. These arise due to the thickness of the disk. In addition to the two diffraction points on the front edge of the disk, there is a third diffraction point on the back edge. For the pair of points separated by the disk thickness, we expect an interference pattern of vertical bands spaced by $c/2d$= 300 / (2 x 20.4 ) = 7.35 GHz, corresponding to the vertical dark bands seen at about 7.5 and 15 GHz in Fig. 7(a).

For vertical polarization in Fig. 7(b), we see the parallel horizontal bands expected near $\theta = 0$. Near $\theta = -90$ degrees, the edge wave mechanism dominates, and we see a family of ellipses. We can read the spacing of the ellipses from Fig. 7(b) to be about 1.14 GHz, closer than the 1.46 GHz spacing of the pattern of horizontal bands in part (a) of the figure. The edge wave model predicts ellipses that cross the vertical axis with a spacing given by Eqn. (18) of $c/((\pi+2)R) = 300/((\pi+2)x50.45) = 1.16$ GHz, about equal to the value read from Fig. 7(b).

The pattern of ellipses is of greater angular extent at the low end of the frequency band, being visible from $\theta = -90$ degrees to angles of -30 or even -20 degrees. As the frequency increases, the angular extent of the pattern diminishes, so that near 18 GHz the pattern is clearly seen only for $-105 \le \theta \le -75$ degrees, 15 degrees away from edge-on incidence. The pattern of ellipses has an almost constant arc-length, and is reminiscent of the constant width of the bright band associated with specular reflection, discussed above in conjunction with scattering from the strip.

The pattern of ellipses is sharp along $\theta = -90$ degrees from 2 to about 6 GHz, but becomes increasingly blurred as the frequency approaches 18 GHz. The edge wave mechanism is quite frequency dependent, with the wave shedding more of its energy as it travels around the edge at higher frequencies. Hence at higher frequencies the wave has less energy to scatter back in the direction of the incident wave, and the interference pattern is less distinct.

### 4.3 The Cone for Vertical Polarization

The small metallic cone in Fig. 2(f) has half-angle 39.85 degrees, base diameter 29.8 mm, and length 17.85 mm. The cone was positioned with its main axis on the $x$ axis. In this orientation the base of the cone lies in a $yz$ plane. The RCS was measured with the incident wave vertically polarized, from 2 to 18 GHz, and is shown in Fig. 8. There is a strong specular reflection around $\theta = 180$ degrees, when the wave is normally incident on the cone's base. There is also a weaker specular reflection from the curved surface of the cone, near $\theta = 50$ degrees. The pattern of light and dark bands between $\theta = 70$ degrees and $\theta = 130$ degrees have the elliptical shape characteristic of edge wave scattering.

We might expect to see a pattern of horizontal bands near $\theta = 180$ degrees, due to interference of the fields diffracted from two diametrically opposite points on the cone's edge. The expected spacing would be $c/(2d) = 300 / (2 \times 29.8) =$ 5.0 GHz. There is a hint of dark horizontal bands of minimum RCS intersecting the 18 GHz outer circle at about 140 degrees and at about 160 degrees and 200 degrees, but the target is too small to produce a clear pattern. The spacing is about 5 GHz as expected.

To compare the location of the measured ellipses of minimum RCS in Fig. 8 with those predicted by our simple interference theory and Eqn. (18), Fig. 13 was drawn using the small cone's base radius of 14.9 mm. The phase change associated with diffraction from the edge was estimated using the "soft" diffraction coefficient[9], $D_s$, for a straight edge with a wedge of angle 50 degrees, and incidence at $\theta = 90$ degrees, to obtain $\alpha_1 = 135$ degrees. The phase change associated with the edge wave was estimated using the thin disk expression given by Eqn. (14) in Ref. [14]. This equation includes the phase change of $-k\pi R$ associated with the distance traveled by the edge wave. In addition to some phase terms that are constant with frequency, there is a phase change associated with $-\alpha_i \pi R$, where[14]

$$\alpha = \alpha_r + j\alpha_i = 0.5k(kR)^{-2/3}e^{-j\pi/6} \qquad \ldots(19)$$

Thus the phase change associated with the edge wave, $\alpha_2$, is not constant with frequency, but instead includes a term proportional to $f^{1/3}$. Eqn. (14) in Ref. [14] was evaluated for the cone's base radius of 14.9 mm. It was found that $\alpha_2$ varies from -154 degrees at 2 GHz to -112 degrees at 18 GHz; a representative value of -136 degrees was chosen to plot Fig. 13.

Fig. 13 shows the curves of minimum RCS expected for the small cone, plotted from 2 GHz at the inner circle to 18 GHz at the outer. The curves in Fig. 13 are quite similar to the dark bands of minimum RCS seen in Fig. 8, from about 70 to about 130 degrees. The expected curves in Fig. 13 cross the vertical axis at 2.9, 6.9, 10.8 and 14.7 GHz. This corresponds quite well to the frequencies where the dark bands cross the vertical axis in Fig. 8, of about 6.3, 10.5 and 14.4 GHz. The curve expected at 2.9 GHz is not seen in Fig. 8.

Another example of edge wave scattering can be seen in Fig. 5(a) of Ref. [8]. The figure shows a polar color map for the RCS with vertical polarization of a large right-circular cone of base diameter 83.6 mm, length 50.0 mm, and half angle 40 degrees. The base diameter is much larger than that of the 29.8 mm cone used for Fig. 8, and comparable in size to the thick disk discussed above. The polar color map in Ref. [8] Fig. 5(a) shows a striking pattern of ellipses between $\theta = 60$ degrees and 140 degrees. There are 11 maxima along the vertical axis, spaced about 1.45 GHz apart. This agrees reasonably well with Eqn. (18), which predicts a spacing of 1.40 GHz.

## 5. CONCLUSION

This paper presented the measured RCS of six simple targets as a color map in polar coordinates. Such "polar color maps" show striking patterns of bright and dark bands. In each angular range, these patterns arise due to interference between two or three scattered waves: two or three edge diffractions; two edge diffractions plus a tip diffraction; a reflection plus a tip diffraction; or an edge diffraction plus an edge wave. The identification of primary scattering mechanisms by recognizing patterns on polar color maps provides the RCS specialist with an effective diagnostic and educational tool.

Not discussed in this paper is the effect of target resonance[15] in a polar color map. The resonant frequencies of a structure are independent of the angle of incidence of the plane wave, hence give rise to RCS maxima and minima at constant radius on a polar color map. However, the degree to which the resonance is excited does depend on the angle of incidence. Hence, resonance on a polar color map leads to circles whose intensity varies with incidence angle. Fig. 8 in Ref. [8] shows the RCS of a rod with an attached wire; the wire is resonant when its length is approximately equal to odd multiples of the quarter-wavelength. The color map clearly shows resonance circles.

RCS data as a function of frequency and of incidence angle are often used with two-dimensional signal processing techniques to draw a rectangular-format color contour map of the intensity of the return as a function of distance, down-range and cross-range[16]. Such maps show strong returns from localized scattering sources such as the wing-tips of an aircraft, and the resulting images bear a shadowy resemblance to the target. The techniques presented here may be complementary in that specific scattering mechanisms not associated with point-source scattering are readily identified.

Methods and computer codes in computational electromagnetics become established as useful analysis tools by "code validation": the building of an "experience base" of problems solved and compared with reference data. The conclusions drawn from code validation should be stated as "modeling guidelines"[17] which provide rules-of-thumb for constructing a model for solution by that computational method, and specify geometrical restrictions on the input geometry which respect the limitations on the validity of the CEM code. The usefulness of a CEM code for solving a new problem, perhaps by an inexpert user, is closely related to the quality and explicitness of the associated modeling guidelines.

Modeling guidelines are best developed by comparing computations with measurements as a function of frequency over a wide range, as well as by examining individual radiation or scattering patterns at single frequencies. Although calculating the RCS as a function of both frequency and incidence angle is a massive computation, comparing measured and computed polar color maps of the RCS provides a comprehensive evaluation of the performance of a computer code for a given problem, and may be useful for formulating modeling guidelines. This paper has related features on a polar color map, such as lines, hyperbolas, and ellipses, to the scattering mechanisms of the target, and may provide insight into the cause of features seen or missing from computed RCS maps compared to the measured RCS.

Our own code validation studies have compared computations of the monostatic RCS with our measurements[5,6,15,18]. It was noted above that the differences in the computed and measured RCS are largest in the sharp, deep minima, and that this is expected due to the measurement geometry. Because our scattered field measurements are bistatic, and are made at a finite range from the horns, our data is most valuable for code validation when the scattered field due to a point source is computed at the location of the receive horn in Fig. 1. Simulating the measurement setup explicitly in the computation, rather than computing backscattered field due to plane wave incidence, removes the geometry error as a source of difference in comparing the measurement and the computation.

Our data base contains the measured RCS and the phase of the scattered field for a wide variety of metallic and dielectric targets[7]. Some targets are small enough to be studied by moment methods, by the multiple multipole method, or by the finite-difference time-domain method. Others are so large that ray-tracing would be the natural approach. This extensive data presents a challenge to the computational electromagnetics community for code validation. Our measured data, and the associated plotting software, POLPLOT and other programs, are freely available to the community and can be fetched by ftp from "lucas.incen.doc.ca", or by referring to our world-wide-web page "http://lucas.incen.doc.ca/rcs.html".

## REFERENCES

1. S.J. Kubina and C.W. Trueman, "The Validation of EM Modelling Codes - A User Viewpoint", ***The Applied Computational Electromagnetics Society Journal***, Special Issue on Electromagnetics Computer Code Validation, 1989.
2. R.G. Kouyoumjian, ***The Calculation of the Echo Area of Perfectly Conducting Objects by the Variational Method***, Ph.D. dissertation, The Ohio State University, Columbus, Ohio, November, 1953.
3. E.F. Knott, V.V. Liepa and T.B.A. Senior, "Plates and Edges", ***IEEE Trans. on Antennas and Propagation***, vol. AP-19, no. 6, pp. 788-789, November, 1971.
4. A.D. Yaghjian and R.V. McGahan, "Broadside Radar Cross-Section of the Perfectly-Conducting Cube",

***IEEE Trans. on Antennas and Propagation***, vol. AP-33, no. 3, March, 1985.

5. C.W. Trueman, S.J. Kubina, S.R. Mishra and C. Larose, "RCS of Four Fuselage-Like Scatterers at HF Frequencies", ***IEEE Trans. on Antennas and Propagation***, vol. AP-40, no. 2, pp. 236-240, February 1992.
6. S.R. Mishra, C.L. Larose and C.W. Trueman, "Precision Radar Cross-Section Measurements for Computer Code Validation", ***IEEE Trans. on Instrumentation and Measurement***, vol. 42, no. 2, pp. 179-185, April 1993.
7. S.R. Mishra, C.L. Larose, M. Flynn and C.W. Trueman, "A Database of Measured Data for RCS Code Validation", ***Conference Proceedings of the 10th Annual Review of Progress of the Applied Computational Electromagnetics Society***, Monterey, California, March 21-26, 1994.
8. C.L. Larose, S.R. Mishra and C.W. Trueman, "Graphics for Visualizing RCS as a Function of Frequency and Angle", ***IEEE Antennas and Propagation Magazine***, vol. 36, pp. 7-13, June 1994.
9. A. Balanis, ***Advanced Engineering Electromagnetics***, Wiley, 1989.
10. R.B. Dybdal, "Radar Cross-Section Measurements", ***Proc. IEEE***, vol. 75, pp. 498-516, April, 1987.
11. R.G. Kouyoumjian and L. Peters, "Range Requirements in Radar Cross-Section Measurements", ***Proc. IEEE***, vol. 53, pp. 920-928, August, 1965.
12. S.R. Mishra and C.W. Trueman, "Accuracy of RCS Measurements", ***Proceedings of the 18th Annual Meeting and Symposium of the Antenna Measurement Techniques Association(AMTA)***, Seattle, Washington, Sept. 30-Oct. 4, 1996..
13. M.R. Spiegel, ***Mathematical Handbook of Formulas and Tables***, Schaum's Outline Series, McGraw-Hill, 1968.
14. A.K. Dominek, "Transient Scattering Analysis for a Circular Disk", ***IEEE Trans. on Antennas and Propagation***, vol. 39, no. 6, pp. 815-819, June 1991.
15. C.W. Trueman, S.J. Kubina, S.R. Mishra and C. Larose, "RCS of Scatterers with Attached Wires", ***IEEE Trans. on Antennas and Propagation***, Vol. 41, No. 3, pp. 351-355, March 1993.
16. E.K. Walton, I.J. Gupta, M.W. Tu and A. Moghaddar, "Super Resolution Radar Target Imaging of Realistic Targets", ***Proceedings of the 14th Annual Meeting and Symposium of the Antenna Measurement Techniques Association(AMTA)***, pp. 6-28 to 6-32, Oct. 19-23, 1992.
17. C.W. Trueman and S.J. Kubina, "Verifying Wire-Grid Model Integrity with Program CHECK", ***Applied Computational Electromagnetics Society Journal***, vol. 5, no. 2, Winter, 1990, pp. 17-42.
18. C.W. Trueman, S.J. Kubina, S.R. Mishra and C. Larose, "RCS of a Generic Aircraft at HF Frequencies", ***Canadian Journal of Electrical and Computer Engineering***, Vol. 18, No. 2, pp. 59-64, April 1993.